Available online at www.sciencedirect.com
ScienceDirect
Journal of Computational Physics 226 (2007) 1234–1255
JOURNAL OF COMPUTATIONAL PHYSICS
www.elsevier.com/locate/jcp

A spectral vanishing viscosity for the LES of turbulent flows within rotating cavities

E. Severac, E. Serre *

MSNM-GP UMR6181 CNRS-Aix-Marseille Universite, IMT, Technopole de Chateau-Gombert, 38 rue Joliot-Curie, 13451 Marseille, France

Received 26 July 2006; received in revised form 3 April 2007; accepted 23 May 2007
Available online 8 June 2007

Abstract

A spectral vanishing viscosity technique (SVV) is presented for the simulation of 3D turbulent incompressible flows within a rotor–stator cavity. One characteristic of this technique is that the SVV is active only for the short length scales, a feature which is reminiscent of Large Eddy Simulation models. The Spectral Vanishing Viscosity, first introduced by E. Tadmor for the inviscid Burgers equation [E. Tadmor, Convergence of spectral methods for nonlinear conservation laws, SIAM J. Numer. Anal. 26 (1) (1989) 30], is incorporated into the cylindrical Navier–Stokes equations written in velocity pressure formulation. The second-order operator involved in the SVV-method is implemented in a Chebyshev-collocation Fourier–Galerkin pseudo-spectral code. The SVV is shown to lead to stable discretizations without sacrificing the formal accuracy, i.e., exponential convergence, in the proposed discretization. LES results are presented here for rotational Reynolds numbers ranging from $Re = 7 \times 10^4$ to $Re = 7 \times 10^5$. Turbulent quantities are shown to compare very favorably with results of direct numerical simulation (DNS) and experimental measurements.

Keywords: Spectral vanishing viscosity; Large eddy simulation; Spectral method; Rotating flows

1. Introduction

The simulation of turbulent flow in rotating cavities is a major issue in computational fluid dynamics for engineering applications such as designing rotational machinery, e.g., turbines and compressors, electrical machinery and generator rotors (see the review of Owen and Rogers [1]). The flow between a rotating disk and a fixed parallel disk has received much attention because it serves as a model problem for rotor–stator flow and because rotating disk flow is known to be one of the simplest cases where the turbulent boundary layers are three-dimensional (3D). Thus, this flow is well suited to investigate the effects of mean flow three-dimensionality on the turbulence and its structure [2–4]. Within an enclosed rotor–stator cavity a characteristic feature is the coexistence of adjacent coupled flow regions that are radically different in terms of the

* Corresponding author. Tel.: +33 491118535; fax: +33 491118502.
E-mail address: Eric.Serre@L3M.univ-mrs.fr (E. Serre).

0021-9991/$ - see front matter
doi:10.1016/j.jcp.2007.05.023

flow properties and the thickness scales of the boundary layers (adjacent to the rotating and fixed disks) compared with those of the geostrophic core region [5]. Moreover, the confinement, the flow curvature and the rotation effects create a strongly inhomogeneous and anisotropic turbulence.

Consequently, these flows are very challenging for numerical modeling particularly in turbulent regimes relevant to industrial conditions.

At present, computer performance only permits direct numerical simulation (DNS) of transitionally turbulent cavity flows ($Re = O(10^5)$) [6–8]. Attempts to compute turbulent rotor–stator flows using statistical approaches (Reynolds Averaged Navier–Stokes) has had only partial success. Indeed, the turbulence model must be able to solve the low-Reynolds number regions not only near the disks but also in the core of the flow. Moreover, the model has to predict precisely the location of the transition from the laminar to the turbulent regime, even though it is bounded by instabilities, and so cannot be completely represented by a steady flow model [9]. Second-order closures could be a more appropriate level of closure to predict such complex flows, but even if they provide the correct distribution of laminar and turbulent regions, the Reynolds stress behaviour is not fully satisfactory, particularly near the rotating disk (see for example the work of Launder and Tselepidakis [10]). Consequently, large eddy simulation (LES) may constitute a valuable way to compute such flows.

There is now consensus that LES based on Subgrid-Scale (SGS)-models is subject to fundamental limitations particularly in the case of complex flows. Indeed, traditional SGS-models which have been developed and validated performing simulations of simple academic flows, must be adapted to fully capture the physical complexity. It has been shown for various flows that the shear stress and strain tensors involved in SGS-models have different topological features. In particular, it was reported by Borue and Orzag [11] in the case of numerical simulations of three-dimensional forced homogenous turbulence that the energy flux only weakly correlates with the locally averaged energy dissipation rate, an assumption employed in most eddy-viscosity models (see a review in Lesieur and Métais [12]). To this end, alternative LES formulations have been investigated based on either the filtered or the original Navier–Stokes equations. A filtered non-eddy viscosity approach is the scale-similarity model introduced first by Bardina et al. [13] which assumes that the unknown subgrid-scale stress tensor can be approximated by a stress tensor calculated from the resolved filter employing additional filtering with the filter width equal to or larger than the one used to obtain the original resolved field. However, the low pass filter cuts out the higher frequencies, that will be modelled within the stress tensor, and creates an increase in the energy of the last resolved frequencies (known as the aliasing effect) that usually leads to divergence (see Stolz et al. for ADM filtering and stabilisation [14]). Mixed models that include a dissipative component for numerical stability have been found to provide LES results better than those obtained with the classical Smagorinsky model with the additional benefit of accounting for the backscatter [15]. However, the results do not dramatically improve, and the dependence of the models on a filter introduces an additional complication. Moreover, such mixed models are typically computationally more expensive. As a consequence, only two investigations of turbulent rotating disks flows have provided useful results, using LES based on filtered Navier–Stokes equations. Wu and Squires [16] performed LES of the 3D turbulent boundary layer over a free rotating disk at $Re = 6.5 \times 10^5$ and in an otherwise quiescent incompressible fluid using periodic boundary conditions both in the radial and tangential directions. Lygren and Andersson [20] performed LES in a sector of a rotor–stator cavity assumed homogeneous in the radial direction, for Reynolds numbers ranging from $Re = 4 \times 10^5$ to $Re = 1.6 \times 10^6$. These authors used different dynamical models to model the subgrid-scale stress arising from the filtering operation: the eddy-viscosity model of Germano et al. [17], the mixed model of Zang et al. [18] and the mixed model of Vreman et al. [19]. Their results have offered new evidence to support the observations of Little and Eaton [4] that the mean flow three-dimensionality affects the near-wall vortices and their ability to generate shear-stresses.

Due to the difficulties encountered by the above procedures, there has been an effort for more than 10 years to employ the original (unfiltered) Navier–Stokes equations, invoking nonlinear limiters that implicitly act as a filtering mechanism for the small scales as in the MILES approach [23] or adding an assumption for stabilization [17]. Then, LES modifies the Navier–Stokes equations in order to obtain a new system of equations which is more amenable to approximate, while retaining all the most energetic features of the unperturbed problem.

A spectral vanishing viscosity (SVV) is proposed here as an efficient stabilization technique of our highly accurate spectral method (Chebyshev–Chebyshev–Fourier) developed for DNS of the transitional regimes [5,26]. High Reynolds number flows are difficult to compute when using spectrally accurate numerical schemes. This results directly from the fact that spectral approximations are much less diffusive than low order ones, leading to an accumulation of the energy on the high spatial frequencies which finally leads to the divergence of the computations [24]. Contrary to many stabilization techniques that generally destroy the spectral accuracy of the algorithm [22], SVV possesses the property of preserving the spectral accuracy. It consists in introducing a viscous term acting only on the highest resolved frequencies. SVV was first introduced by Tadmor [27] to solve non-linear hyperbolic equations, typically the Bürgers equation, using standard Fourier spectral methods. Tadmor [27] showed that this artificial dissipation is sufficiently large to suppress oscillations, yet small enough to keep the accuracy. The non-periodic case was then considered in the framework of Legendre discretization by Maday et al. [28], and in the framework of Chebyshev discretization by Andreassen et al. [29], this last one using SVV for two-dimensional simulation of waves in a stratified atmosphere. A formulation of the method for spectral/*hp* Galerkin element has been proposed by Karamanos and Kardianakis [30] and more recently by Kirby and Sherwin [31] who showed the effectiveness of the SVV for the LES of incompressible turbulent flows. A formulation of the method for spectral element approximations has also been proposed by Pasquetti and Xu [32] and validated in the computation of the two-dimensional turbulent wake of a cylinder. Further extensions have been proposed based on the introduction of a spectral hyperviscosity term which presents additional interesting mathematical properties including the uniqueness of the solution (which is still an open question for the SVV) [22]. Nevertheless, in practice the SVV, which involves a second-order operator only, is more readily implemented in standard codes.

In the current work, we show the capabilities of the SVV to act as a LES when it is implemented in a Navier–Stokes spectral code for investigating rotating turbulent flows with walls. In Section 2 mathematical modelling and numerical approximation are presented. Then, the SVV is extended in Section 3 to an original formulation for the Navier–Stokes equations in cylindrical geometry. Analytical results are shown in Section 4 concentrating on preserving spectral accuracy. In Section 5, the SVV is used to compute annular rotor–stator flows, firstly at a relatively low-Reynolds number, $Re = 7 \times 10^4$, in order to validate the results with DNS (Section 5.1), and secondly at high rotation rates ($Re = 4 \times 10^5$ and $Re = 7 \times 10^5$) where turbulent quantities are compared with experimental measurements (Section 5.2). Finally, some concluding remarks are given in Section 6.

2. Mathematical modelling and numerical approximation

2.1. Mathematical modelling

We consider the flows contained between two disks enclosing an annular domain of radii a and b with $b > a$ and bounded by two co-axial cylinders of height $2h$. One disk of the cavity is stationary (stator) and the other (rotor) rotates at uniform angular velocity $\Omega = \Omega e_z$, e_z being the unit vector on the axis (see Fig. 1).

The incompressible fluid motion is governed by the three-dimensional Navier–Stokes equations which are written below in primitive variables.

$$\frac{\partial \mathbf{V}}{\partial t} = \nu \Delta \mathbf{V} - (\mathbf{V} \cdot \nabla \mathbf{V}) - \nabla p + \mathbf{F} \quad \text{in } D \tag{1}$$

$$\mathbf{V} = \mathbf{W} \quad \text{on } \Gamma = \partial D \tag{2}$$

$$\nabla \cdot \mathbf{V} = 0 \quad \text{in } \overline{D} = D \sqcup \Gamma \tag{3}$$

where t is the time, $\mathbf{V}$ is the velocity of components (u, v, w) in the radial, azimuthal, and axial directions respectively, for cylindrical coordinates (r, θ, z), p is the pressure and $\mathbf{F}$ represents a given body force. Eqs. (1)–(3) are completed by specific initial conditions for the velocity:

$$\mathbf{V} = \mathbf{V}_0 \quad \text{with } \nabla \cdot \mathbf{V}_0 = 0 \quad \text{in } \overline{D} \tag{4}$$

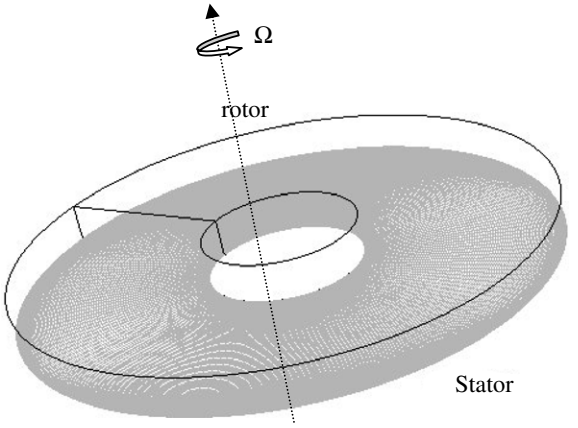

Fig. 1. Scheme of an annular rotor–stator cavity.

∇ is the vectorial Laplacian operator written for cylindrical coordinates:

$$(\Delta V)_{\mathrm{r}} = \nabla^2 u - \frac{u}{r^2} - \frac{2}{r^2}\frac{\partial v}{\partial \theta} \tag{5}$$

$$(\Delta V)_{\theta} = \nabla^2 v - \frac{v}{r^2} + \frac{2}{r^2}\frac{\partial u}{\partial \theta} \tag{6}$$

$$(\Delta V)_{z} = \nabla^2 w \tag{7}$$

with

$$\nabla^2 = \frac{\partial^2}{\partial r^2} + \frac{1}{r}\frac{\partial}{\partial r} + \frac{1}{r^2}\frac{\partial^2}{\partial \theta^2} + \frac{\partial^2}{\partial z^2} \tag{8}$$

Cylindrical coordinates induce coupling between first two components of the vectorial Laplacian. A variable transformation is used to make it diagonal [39]:

$$u_+ = u + \mathrm{i}v, \quad u_- = u - \mathrm{i}v \quad (\mathrm{i}^2 = -1) \tag{9}$$

so that the vectorial Laplacian becomes diagonal with

$$(\Delta V)_{+} = \left(\nabla^2 - \frac{1}{r^2} + \frac{2\mathrm{i}}{r^2}\frac{\partial}{\partial \theta}\right) u_+ \tag{10}$$

$$(\Delta V)_{-} = \left(\nabla^2 - \frac{1}{r^2} - \frac{2\mathrm{i}}{r^2}\frac{\partial}{\partial \theta}\right) u_- \tag{11}$$

$$(\Delta V)_{z} = \nabla^2 w \tag{12}$$

2.2. Projection scheme for time-discretization and space approximation

Eqs. (1)–(3) are solved for the new complex variables (u_+, u_-, w) defined in Eq. (9) and constitute a Stokes problem coupling the velocity and the pressure.

The temporal discretization adopted in this work is a projection scheme, based on backwards differencing in time [25,26]. The projection scheme requires the solution of a pressure Poisson equation to (approximately) maintain solenoidality of the velocity. The details of our algorithm lies in the computation at each time step of a pressure predictor (through this pressure Poisson equation is augmented with a pressure Neumann boundary condition obtained by projection of the momentum equation on the domain normal), which allows the correct temporal evolution of the normal pressure gradient at the boundaries during the time integration.

Eqs. (1)–(3) are discretized in time using a second-order semi-implicit scheme which combines a implicit treatment of the diffusive term and an explicit Adams–Bashforth extrapolation for the non-linear convective terms. The unsteady term is approximated by a second-order backward Euler finite-difference scheme. Its good stability properties for an advection–diffusion equation have been shown before by Vanel et al. [33].

In the non-homogeneous radial and axial directions (r,z) a collocation Chebyshev approximation is used, associated with Gauss–Lobatto collocation points $(Y_i,Z_j), i=0,\ldots,N_1$ and $j=0,\ldots,N_3$ defined in the square $[-1,1]$. The natural strenghtening of these points near the boundaries is well adapted to the description of the thin boundary layers which develop at the walls in the meridian plane. A standard Fourier–Galerkin approximation is employed for the solution in the 2π-periodic tangential direction. Then, for each Fourier mode, the solution $(\mathbf{V},p)$ is approximated by Chebyshev polynomials of degree at most equal to N_1 in the radial direction and to N_3 in the axial direction. We note that $N_2/2$ is the cut off frequency of the Fourier series.

Therefore, the approximate solution of $\Psi=(u_+,u_-,w,p)$ is then expressed as:

$$\Psi_{N_1N_2N_3}(Y_i,\theta_q,Z_j,t)=\sum_{k=-N_2/2}^{N_2/2-1}\sum_{n=0}^{N_1}\sum_{m=0}^{N_3}\widehat{\Psi}_{nkm}(t)T_n(Y_i)T_m(Z_j)\mathrm{e}^{\mathrm{i}k\theta_q}, \tag{13}$$

with $-1\leqslant Y_i,Z_j\leqslant 1,\ 0\leqslant\theta\leqslant 2\pi$, where $\widehat{\Psi}_{nkm}$ are the spectral coefficients and $\theta_q=2\pi q/N_2$, with $0\leqslant q\leqslant N_2-1,\ 0\leqslant i\leqslant N_1,\ 0\leqslant j\leqslant N_3$.

For the computation of the non-linear terms, a pseudo-spectral technique is used. Specifically, the derivatives in each direction are calculated in the spectral space and the products are calculated in the physical space as presented in the book of Peyret [24]. A FFT algorithm is used to connect the spectral and the physical spaces. On the other hand, the implicit diffusive term is evaluated through spectral differentiation matrices [24].

Finally, for each Fourier mode, a full diagonalization technique is used for solving a set of 2D uncoupled Helmholtz and Poisson problems (see a detailed analysis in Serre and Pulicani [25]).

3. SVV incorporation into the Navier–Stokes equations

The SVV-operator is incorporated into the projection scheme to discretize the incompressible Navier–Stokes equations (Eqs. (1)–(3)). In the frame of collocation methods, an appropriate viscosity operator, only active for high wave numbers of the numerical approximation, is incorporated in the Helmholtz equations of the velocity prediction.

3.1. Definition of the SVV-operator

According to the pioneering work of Tadmor [27], the SVV-operator in the one-dimensional (1D) case reads in discrete forms as:

$$\widetilde{\Delta_N}\equiv\varepsilon_N\partial_x(Q_N\partial_x u_N), \tag{14}$$

with N for the discretization parameter and $u_N(x)$ for the approximation of u.

In Eq. (14), $\varepsilon_N(\to 0)$ is a viscosity amplitude and Q_N, which is in general a function of x, is the spectral viscosity operator only activated for high wavenumbers.

In Fourier space, this kind of spectral viscosity can be efficiently implemented as multiplication of Fourier coefficients $\widehat{u}_N$with the Fourier coefficients of the kernel $\widehat{Q}_N$, i.e.:

$$\varepsilon_N\partial_x(Q_N\partial_x u_N)=-\varepsilon_N\sum_{k_T\leqslant|k|\leqslant N}k^2\widehat{Q}_k\widehat{u}_k\,\mathrm{e}^{\mathrm{i}kx}, \tag{15}$$

where k is the wavenumber, N is the number of Fourier modes, and k_T the wavenumber above which the spectral vanishing viscosity is active.

This definition (Eq. 15) may be extended in Chebyshev space for any function Φ and its approximation Φ_N, such that in the 1D non-periodic case:

$$\Phi_N = \sum_{k=0}^{N} \widehat{\Phi}_k T_k \tag{16}$$

$$Q_N(\Phi_N) \equiv \sum_{k=0}^{N} \widehat{Q}_k \widehat{\Phi}_k T_k \tag{17}$$

where $\{T_k\}$ is a set of Chebyshev polynomials.

There is not a direct way to extend the definition given by Eq. (14) to the 3D case as shown by the different forms proposed in the literature [30,32]. According to these forms, the following definition was used here:

$$\widetilde{\Delta_N} \equiv \cdot(\varepsilon_N Q_N(\nabla \mathbf{V}_N)), \tag{18}$$

where $\mathbf{V}_N$ denotes the approximation of the velocity vector $\mathbf{V}$, $\nabla \mathbf{V}_N$ is the Jacobian of the vectorial function $\mathbf{V}_N = (u_{N_1N_2N_3}, v_{N_1N_2N_3}, w_{N_1N_2N_3})$. Moreover, $\varepsilon_N Q_N \equiv \mathrm{diag}\{\varepsilon^i_{N_i} Q^i_{N_i}\}$ with $i = 1, 2, 3$ (corresponding to the r, θ, z, directions respectively), where $\varepsilon^i_{N_i}$ is the maximum of viscosity and $Q^i_{N_i}$ 1D viscosity operator acting in direction i.

The viscosity amplitude $\varepsilon^i_{N_i}$ is usually a $\mathrm{O}(1/N_i)$ coefficient, based on the work of Maday et al. [28] who used for Legendre pseudo-spectral methods $\varepsilon^i_{N_i} = 1/N_i$.

The 1D viscosity operator acting in direction i, $Q^i_{N_i}$, is defined in the spectral space (Fourier or Chebyshev) by the smooth function [28]: $\widehat{Q}^i_{N_i}(\omega) = 0$, if $0 \leqslant \omega \leqslant \omega_{T_i}$ and $\widehat{Q}^i_{N_i}(\omega) = \exp(-(\omega - \omega_{N_i})^2/(\omega - \omega_{T_i})^2)$ if $\omega_{T_i} < \omega \leqslant \omega_{N_i}$, where ω_{T_i} and ω_{N_i} are the threshold frequencies after which the viscosity is applied and the highest frequency calculated in the direction i, respectively. Modes are usually activated in the literature for $\omega \geqslant \omega_{T_i} = \mathrm{O}(\sqrt{N_i})$ as for example in Maday et al. [28] where $\omega_{T_i} = 5\sqrt{N_i}$.

A plot of the viscosity kernel normalized by its maximum value at $\omega = N_i$ is shown in Fig. 2 for different values of the cutoff wave number $\omega_{T_i} = C\sqrt{N_i}$, $C = 0$, $C = 1$, $C = 5$. This range has been used in most of the numerical experiments so far (see for example Refs. [28,30,32]) and it is consistent with the theoretical results of Tadmor [27].

Fig. 2 shows that the SVV-operator affects at most the two-third of the spectrum at the highest frequencies ($\omega_{T_i} = 0$) and consequently, DNS results are easily recovered for laminar flows, contrary to some classical LES techniques such as, for example, with the well-known spectral eddy-viscosity model of Kraichnan [34] used by Lesieur's group [12].

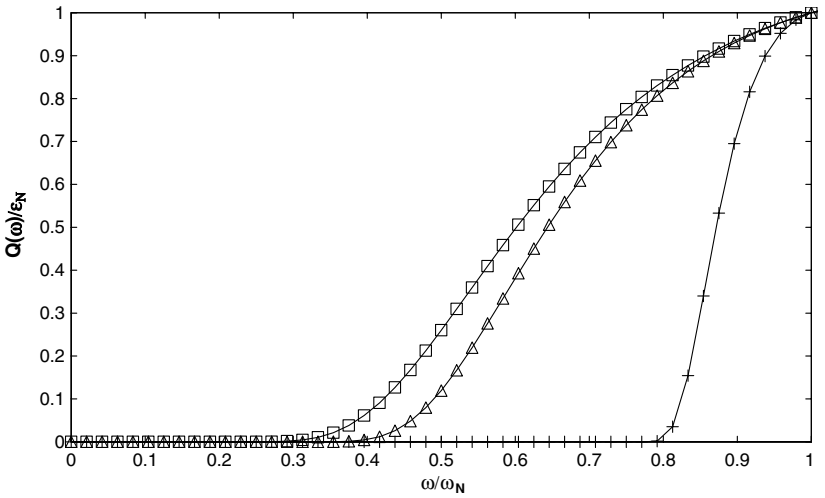

Fig. 2. Normalized viscosity kernels for the spectral vanishing viscosity operator for three different threshold frequencies (crosses $\omega_T = 5\sqrt{N}$, white triangles $\omega_T = \sqrt{N}$ and white squares $\omega_T = 0$).

As the spectral eddy-viscosity is generally used with spectral methods, it may be of interest to mention here that the viscosity operator is identical in both approaches. The major difference lies in the scaling of the viscosities and in the definition of the non-dimensional viscosity laws. Nevertheless, since Kraichnan's eddy-viscosity does not vanish in the low mode region, this approach destroys the spectral accuracy of the numerical method (see a proof in the work of Guermond et al. [22]).

3.2. SVV implementation

The pressure predictor step is not modified by our SVV implementation and the pressure Poisson equation remains the same as that used by Raspo et al. [26]. Thus,

$$\nabla^2 p^{*,n+1} = \nabla \cdot (-2(\mathbf{V}\cdot\nabla\mathbf{V})^n + (\mathbf{V}\cdot\nabla\mathbf{V})^{n-1} + \mathbf{F}^{n+1}) \quad \text{in } D \tag{19}$$

with pressure boundary condition

$$\partial_n p^{*,n+1} = \mathbf{n}.\begin{pmatrix} (-3\mathbf{W}^{n+1} + 4\mathbf{V}^n - \mathbf{V}^{n-1})/2\delta t \\ -2(\mathbf{V}\cdot\nabla\mathbf{V})^n + (\mathbf{V}\cdot\nabla\mathbf{V})^{n-1} \\ +\nu(2\nabla\times\nabla\times\mathbf{V}^n - \nabla\times\nabla\times\mathbf{V}^{n-1}) + \mathbf{F}^{n+1} \end{pmatrix} \quad \text{on } \Gamma \tag{20}$$

where $\mathbf{n}$ is the domain unit outward normal, and where the Laplacian, approximated using an Adams–Bashforth extrapolation, has been reduced to its irrotational part (the solenoidal one being zero) in order to satisfy the compatibility condition.

The previous step is completed by the calculation of a predicted velocity field $\mathbf{V}^*$ through the solution of a Helmholtz (elliptic) equation where a viscous correction is applied:

$$\nu\Delta_{\mathrm{SVV}}(\mathbf{V}^*) - \frac{3}{2\delta t}\mathbf{V}^* = \begin{pmatrix} (-4\mathbf{V}^n + \mathbf{V}^{n-1})/2\delta t + 2(\mathbf{V}\cdot\nabla\mathbf{V})^n \\ -(\mathbf{V}\cdot\nabla\mathbf{V})^{n-1} + \nabla p^{*,n+1} - \mathbf{F}^{n+1} \end{pmatrix} \quad \text{in } D \tag{21}$$

with appropriate velocity boundary conditions at time $(n+1)t$.

The new diffusion operator Δ_{SVV} can be simply implemented by combining the classical diffusion and the new SVV terms to obtain:

$$\nu\Delta_{\mathrm{SVV}} \equiv \nu\Delta + \nabla\cdot(\varepsilon_N Q_N \nabla) = \nu\nabla\cdot S_N\nabla \tag{22}$$

where ν is the diffusive coefficient and where

$$S_N = \mathrm{diag}\{S^i_{N_i}\}, \quad S^i_{N_i} = 1 + \frac{\varepsilon^i_{N_i}}{\nu} Q^i_{N_i} \tag{23}$$

with $\varepsilon^i_{N_i}$ the maximum of viscosity and $Q^i_{N_i}$ the 1D viscosity operator acting in direction i, and previously defined in Section 3.1.

Notice that in Eq. (22) the SVV term is not scaled by the Reynolds number, since the kinematic viscosity only scales the diffusion term. Consequently, for a fixed grid and given SVV parameters, the SVV term becomes larger relatively to the classical diffusion term when increasing Reynolds number.

Denoting the partial derivative ∂_i in the direction i, as

$$\widetilde{\partial}_i \equiv S^i_{N_i}\partial_i, \tag{24}$$

in the cylindrical coordinate system (r,θ,z), we obtain an expression of the scalar Laplacian in the basis (u,v,w):

$$\nabla^2_{\mathrm{SVV}} = \partial_{\mathrm{r}}\widetilde{\partial}_{\mathrm{r}} + \frac{1}{r}\widetilde{\partial}_{\mathrm{r}} + \frac{1}{r^2}\partial_\theta\widetilde{\partial}_\theta + \partial_z\widetilde{\partial}_z \tag{25}$$

In the Fourier spectral space, with k for azimuthal wave number and $\widehat{S}^2_{N_2}$ for the corresponding coefficient of the SVV-operator in the azimuthal direction, this yields:

$$k\in[1,\ldots,N_2], \quad \nabla^2_{\mathrm{SVV},k} = \partial_{\mathrm{r}}\widetilde{\partial}_{\mathrm{r}} + \frac{1}{r}\widetilde{\partial}_{\mathrm{r}} - \frac{\widehat{S}^2_{N_2}}{r^2}k^2 + \partial_z\widetilde{\partial}_z \tag{26}$$

Using now the new set of complex variables (u_+, u_-, w) introduced above, we obtain for the azimuthal wavenumber k an expression of the modified vector Laplacian, k in $[1, \ldots, N_2]$:

$$\nabla^2_{\mathrm{SVV},k} = \left(\widetilde{\partial}_{\mathrm{r}}\widetilde{\partial}_{\mathrm{r}} + \frac{1}{r}\widetilde{\partial}_{\mathrm{r}} + \widetilde{\partial}_z\widetilde{\partial}_z\right)I - \frac{\widehat{S}^2_{N_2}}{r^2}\mathrm{diag}\{(k+1)^2, (k-1)^2, k^2\} \tag{27}$$

where I is the identity matrix. The last correction step remains unchanged compared with Raspo et al. [26]. The predicted velocity field V^* is corrected by taking into account the pressure gradient at t^{n+1} so that the final velocity field satisfies the incompressibility constraint:

$$\frac{3}{2\delta t}(\mathbf{V}^{n+1} - \mathbf{V}^*) = -\nabla(p^{n+1} - p^{*,n+1}) \quad \text{in } \overline{D} \tag{28}$$

$$\nabla \cdot \mathbf{V}^{n+1} = 0 \quad \text{in } D \tag{29}$$

$$\mathbf{V}^{n+1} \cdot \mathbf{n} = \mathbf{V}^* \cdot \mathbf{n} \quad \text{on } \Gamma \tag{30}$$

This correction is not performed by means of Eqs. (28)–(30) but by computing an intermediate variable $\phi = 2\delta t(p^{n+1} - p^{*,n+1})/3$ from a Poisson problem obtained by taking the divergence of Eq. (28).

Thus, the discretization of the Navier–Stokes equations leads to different uncoupled Helmholtz and Poisson problems like Eqs. (19)–(21) for the pressure and velocity which can be written in matrix form. An efficient way to solve these problems is to use the diagonalization technique, especially for time-dependent problems, when the solution must be computed at each time step in D.

The classical second-order derivatives of the Laplacian operators in cylindrical coordinates for the velocity equation are modified by the implementation of the SVV-operator (unlike the pressure), and Eq. (21) leads to the following matrix system obtained for each k in the Fourier space:

$$A\Psi + \Psi B = S \tag{31}$$

where

$$A = D_1\left(I + \frac{1}{v}\varepsilon^1_{N_1}P^{-1}\mathrm{diag}\left\{\widehat{\mathbf{Q}}^1_{N_1}\right\}_l P\right)D_1 + \frac{1}{r}\left(I + \frac{1}{v}\varepsilon^1_{N_1}P^{-1}\mathrm{diag}\{\widehat{\mathbf{Q}}^1_{N_1}\}_l P\right)D_1 - \sigma_i I, \tag{32}$$

for $i = 1, 2, 3$, $0 \leqslant l \leqslant N_1$, with P the transformation matrix from the physical to the spectral space, and

$$\begin{aligned} \sigma_1 &= \frac{\widehat{S}^2_{N_2}(k+1)^2}{r^2} + \frac{3}{2v\delta t}, \quad \sigma_2 = \frac{\widehat{S}^2_{N_2}(k-1)^2}{r^2} + \frac{3}{2v\delta t}, \\ \sigma_3 &= \frac{\widehat{S}^2_{N_2}k^2}{r^2} + \frac{3}{2v\delta t} \end{aligned} \tag{33}$$

and where

$$B = \left[D_3\left(I + \frac{1}{v}\varepsilon^1_{N_1}P^{-1}\mathrm{diag}\{\widehat{\mathbf{Q}}^3_{N_3}\}_l P\right)D_3\right]^{\mathrm{T}} \tag{34}$$

for $0 \leqslant l \leqslant N_3$, D_1 and D_3 denote the first-order derivative operators in the radial and axial directions, respectively, with $D_1 = [\mathrm{d}r_{ij}]_{i,j\in[1,\ldots,N_1]}$ and $D_3 = [\mathrm{d}z_{ij}]_{i,j\in[1,\ldots,N_3]}$. The coefficients $\mathrm{d}r_{ij}$ and $\mathrm{d}z_{ij}$ can be obtained by using the orthogonality property of the Chebyshev polynomials and the usual trigonometric formulas (see in [40]).

Depending on the range of physical, geometrical and numerical parameters, operators A and B (Eqs. (32) and (34) may no be longer diagonalisable in the real space. Our numerical results show that when the ratio $(a+b)/(b-a)$ becomes smaller than about 2.5 (i.e. when the curvature increases) the second-order derivative of the Laplacian operators in the radial direction for the pressure equation (and thus for the intermediate variable ϕ) may exhibit a large number of complex eigenvalues depending on the resolution. Consequently, this occurrence of complex eigenvalues involves using complex FFT which brings an additional cost in terms of time and memory of about 35% and 95%, respectively.

4. Accuracy of the SVV-method on a 3D analytical solution

Guermond et al. [22] have mathematically shown using a standard Fourier–Galerkin-method that SVV maintains spectral accuracy for nonlinear conservations laws. The purpose here is to demonstrate that the addition of SVV as proposed does not destroy this expected convergence property of the pseudo-spectral method that is being employed. The governing equations (Eqs. (1)–(3)) are made dimensionless using h, $b\Omega$ and Ω^{-1} as characteristic scales for length, velocity, and time, respectively. As usual in the literature on rotor–stator flow, the control parameter is the Reynolds number defined by $Re = \Omega b^2/\nu$ where ν is the kinetic viscosity. Two geometrical parameters are defined: the aspect ratio $L = (b-a)/2h$ and the curvature parameter $R_m = (a+b)/(b-a)$. The tests reported here were performed with $L = 5$, $R_m = 5$ and $Re = 500$. The exact steady solution is defined on $\overline{D} = [-1,+1] \times [0, 2\pi[\times[-1,+1]$ by:

$$\begin{aligned} u_a &= \frac{2}{L(Y+R_m)} z^2 \tanh(1-z^3)\sin\theta\cos 2\theta \\ v_a &= 5\times 10^{-2}(1+2\cdot\ln(L(Y+R_m)))z^2\tanh(1-z^3) \\ w_a &= 2\times 10^{-1}\sin^2(L(Y+R_m)^2)\frac{1+\sin\theta}{2+\cos\theta} \\ p_a &= 10^{-1}\tanh(1-L^2(Y+R_m)^2)z^2\sin z(\sin\theta+\cos 2\theta)^2 \end{aligned} \tag{35}$$

The velocity field $\mathbf{V}_a$ is actually divergence free. From this exact solution, we readily deduce the Dirichlet boundary conditions of the variables and the forcing terms $\mathbf{F}$.

Table 1
Effect of the SVV parameters on the accuracy of the numerical method

N	ε_N	ω_T	$L_\infty(\mathbf{V})$	$L_2(\mathbf{V})$	$L_1(\mathbf{V})$
25	0	0	2.58×10^{-7}	1.15×10^{-7}	8.67×10^{-8}
	$1/2N$	$\sqrt{N}$	5.20×10^{-3}	7.51×10^{-4}	3.29×10^{-4}
	$1/2N$	$N/2$	4.78×10^{-3}	6.33×10^{-4}	2.69×10^{-4}
	$1/2N$	$5\sqrt{N}$	2.57×10^{-7}	1.15×10^{-7}	8.67×10^{-8}
	$1/N$	$\sqrt{N}$	5.03×10^{-3}	2.22×10^{-3}	1.61×10^{-3}
	$1/N$	$N/2$	3.10×10^{-3}	1.26×10^{-3}	8.77×10^{-4}
	$Q=$ cste	–	7.28×10^{-3}	1.80×10^{-3}	1.18×10^{-3}
33	0	0	1.33×10^{-9}	6.06×10^{-10}	4.67×10^{-10}
	$1/2N$	$\sqrt{N}$	2.36×10^{-3}	3.01×10^{-4}	1.21×10^{-4}
	$1/2N$	$N/2$	2.84×10^{-4}	3.83×10^{-5}	1.67×10^{-5}
	$1/2N$	$5\sqrt{N}$	1.94×10^{-6}	3.50×10^{-7}	1.82×10^{-7}
	$1/N$	$\sqrt{N}$	2.21×10^{-3}	8.96×10^{-4}	5.87×10^{-4}
	$1/N$	$N/2$	1.83×10^{-4}	7.64×10^{-5}	5.37×10^{-5}
	$Q=$ cste	–	5.56×10^{-3}	1.39×10^{-3}	9.17×10^{-4}
41	0	0	1.16×10^{-10}	2.17×10^{-11}	1.27×10^{-11}
	$1/2N$	$\sqrt{N}$	6.07×10^{-4}	7.14×10^{-5}	2.72×10^{-5}
	$1/2N$	$N/2$	3.77×10^{-6}	5.13×10^{-7}	2.26×10^{-7}
	$1/2N$	$5\sqrt{N}$	3.82×10^{-9}	6.81×10^{-10}	3.49×10^{-10}
	$1/N$	$\sqrt{N}$	5.79×10^{-4}	2.13×10^{-4}	1.31×10^{-4}
	$1/N$	$N/2$	2.44×10^{-6}	1.02×10^{-6}	7.20×10^{-7}
	$Q=$ cste	–	4.66×10^{-3}	1.13×10^{-3}	7.48×10^{-4}
57	0	0	1.17×10^{-10}	2.16×10^{-11}	1.27×10^{-11}
	$1/2N$	$\sqrt{N}$	8.84×10^{-5}	1.10×10^{-5}	4.34×10^{-6}
	$1/2N$	$N/2$	1.85×10^{-8}	2.65×10^{-9}	1.20×10^{-9}
	$1/2N$	$5\sqrt{N}$	1.18×10^{-10}	2.17×10^{-11}	1.27×10^{-11}
	$1/N$	$\sqrt{N}$	8.51×10^{-5}	3.27×10^{-5}	2.09×10^{-5}
	$1/N$	$N/2$	1.22×10^{-8}	5.29×10^{-9}	3.80×10^{-9}
	$Q=$ cste	–	3.93×10^{-3}	9.50×10^{-4}	6.34×10^{-4}

Analytical solution (Eq. (35)) at $R_m = L = 5$ and $Re = 500$. This solution demonstrates that the addition of spectral vanishing viscosity does not affect the exponential converge of the pseudo-spectral discretization. cste $= 1/10N$.

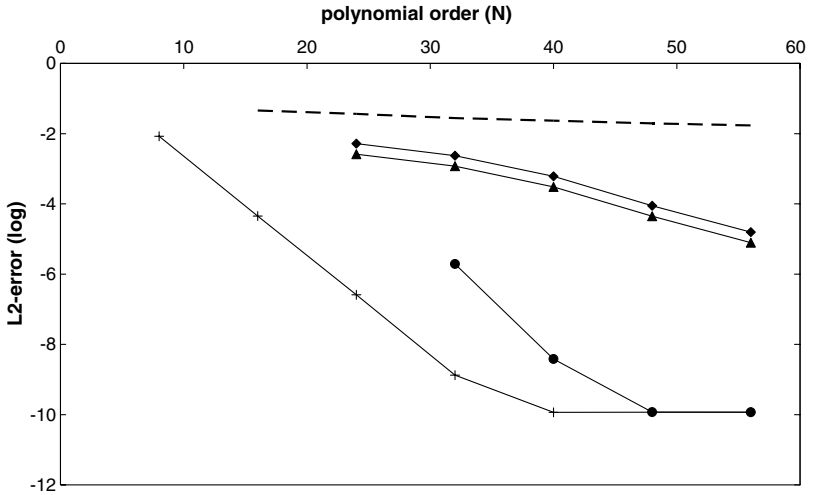

Fig. 3. Consistency behaviour for different sets of SVV parameters ($\omega_T = \sqrt{N}, \varepsilon_N = 1/2N$ (black triangles), $\omega_T = \sqrt{N}, \varepsilon_N = 1/N$ (black diamonds), $\omega_T = 5\sqrt{N}, \varepsilon_N = 1/N$ (black circles)), for DNS (crosses) and for a $O(N^{-1})$ uniform viscous term (dashed line). Logarithm of the L_2-discrete error versus the polynomial order.

The initial condition is the velocity field $\mathbf{V}_a$ perturbed as follows:

$$\mathbf{V}^0 = \mathbf{V}_a + 0.05(Y + R_m)\begin{pmatrix} \sin\theta \\ \cos\theta \\ \sin\theta \end{pmatrix} \tag{36}$$

The spatial accuracy of the algorithm was evaluated by computed the L_1, L_2, and L_∞ discrete errors at the inner collocation points. In this case, the SVV-operator is chosen to be isotropic.

The influence of SVV parameters on the convergence properties of the pseudo-spectral method has been investigated for different polynomial orders. The results are summarized in Table 1 where comparisons of the error at $Re = 500$ with and without SVV are shown. Moreover, the L_2-error versus number of modes is plotted in Fig. 3 for different values of SVV parameters $(\omega_T, \varepsilon_N) = (0,0)$, $(\sqrt{N}, 1/2N)$, $(5\sqrt{N}, 1/2N)$, $(5\sqrt{N}, 1/N)$.

Table 1 clearly shows that even if SVV reduces the accuracy of the solution compared to the reference DNS solution, it does preserve the expected exponential convergence of the approximation developed in DNS. The convergence rate depends on the values of the SVV parameters (see Fig. 3). Of course, uniform viscosity obtained by simply adding a constant $O(N^{-1})$ viscous term on all wavenumbers only yields a first-order algebraic convergence.

The results show the accuracy is more sensitive to the threshold than to the amplitude of the viscous term. Nevertheless, the best results are obtained for the largest value of ω_T ($\omega_T = N/2$ here) and the smallest value of ε_N ($\varepsilon_N = 1/N$).

5. Turbulent rotor–stator flows

Incompressible rotor–stator flows have been investigated in order to demonstrate the capabilities of the SVV-method to capture physics over the range of Reynolds numbers $[7 \times 10^4, 7 \times 10^5]$. SVV results are first compared with DNS results obtained in a transitional turbulent regime at a moderate Reynolds number ($Re = 7 \times 10^4$) in a cavity ($R_m = 5, L = 5$). Then, SVV results are compared with available experimental results of Poncet and Chauve (private communication) in a cavity ($R_m = 1.8, L = 5$) and for two large values of the Reynolds number, $Re = 4 \times 10^5$ and 7×10^5. The experimental measurements were performed using a two component laser Doppler anemometer (LDA). The LDA technique was used to measure the mean radial U

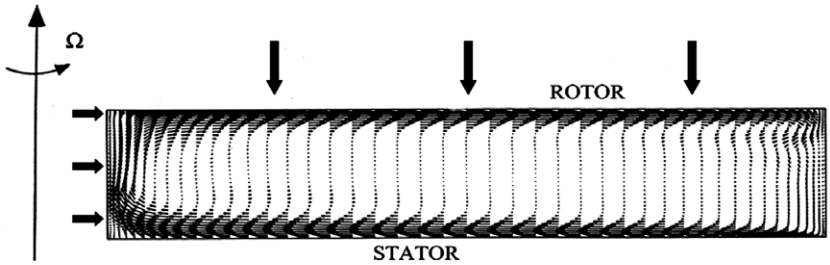

Fig. 4. Base flow of Batchelor type (DNS results). Velocity vector-field in the meridian plane $(r, z, \pi/4)$ at $Re = 10^4$. Black arrows outside the cavity indicate the locations where the flow properties are stored for temporal analyses. Rotor–stator cavity ($R_m = 5, L = 5$).

and tangential V velocities as well as the associated three Reynolds stress tensor components in a meridian plane (r, z) from above the stator. The averaged quantities are written using capital letters.

In the considered range of parameters (Re, L), the rotor–stator flow is characterized by the coexistence of two shear layers next to the disks separated by an inviscid core rotating at constant angular velocity (see this steady axisymmetric Batchelor flow on Fig. 4). The fluid near the rotating disk is driven away from the axis of rotation ($u > 0$) due to centrifugal acceleration and this radial outflow along the rotor is compensated by flow directed towards the inner cylinder ($u < 0$) at the stator side. By analogy with the single disk problem, the boundary layer close to the rotating disk is called the Ekman layer whereas the boundary layer close to the stationary disk is called the Bödewadt layer.

In real situations, the flow between the disks undergoes transition to turbulence when the local Reynolds number $Re_r = \Omega_r^2/\nu$, based on the radial coordinate r, is sufficiently large. The transition process is governed by two generic instabilities, Type I and Type II, arising in both the Bödewadt (stator) and Ekman (rotor) layers. Type I is a crossflow instability, also observed in flow over a swept wing. Type II instability is related to the combined effects of Coriolis and viscous forces. There now exists an extensive literature on transition in these boundary layers characterized by different types of vortex structures, such as rings or spiral arms (see a review in Crespo del Arco et al. [36]). A characteristic of the rotor–stator flow is that the Bödewadt boundary layer is found to be less stable than the rotating Ekman layer [37]. As a consequence, the stator layer becomes turbulent at a lower Reynolds number than the rotor layer. In an experiment with non-merging boundary layers ($R/H = 12.5$), Itoh et al. [37] found that the rotor layer was laminar for $Re_r = 1.6 \times 10^5$, turbulent for $Re_r = 3.6 \times 10^5$ and fully turbulent for $Re_r = 4.6 \times 10^6$. The boundary layer near the stator was found to become turbulent at lower local Reynolds numbers ($Re_r \simeq 2 \times 10^4$). Thus, the structure of these flows is highly complex involving laminar, transitional, and turbulent flow regions.In both cavities no-slip boundary conditions are applied to all walls. Thus, $u = w = 0$; $v = 0$ on the stationary disk, and $v = (R_m + Y)/(R_m + 1)$ on the rotating disk, with $-1 \leqslant Y \leqslant 1$. The inner and outer cylinders that enclose the annular domain may rotate or be at rest, depending on the configuration. The singularity of the tangential velocity at the junction of the stationary cylinders with the rotor (or at the junction between the rotating cylinder and the stator) is regularized by employing a boundary layer function, $v = \exp(-(z-1)/\mu)$, where μ is an arbitrary shape parameter independent of the grid size. Typically, $\mu = 0.006$ has been shown to provide a reasonable representation of experimental conditions (there is a thin gap between the edge of the rotating disk and the stationary sidewall), while retaining spectral accuracy [5]. The calculations are initiated from rest by impulsively spinning up the rotating disk.

5.1. Transition and turbulence in a rotor–stator flow at $Re = 7 \times 10^4$

The flow regime is found to be transitional turbulent characterized by a turbulent stationary disk layer and an unstable laminar rotating disk layer in agreement with former work of the literature (see a review in Serre et al. [7]). At this moderate value of Reynolds number, SVV results fit very well with the DNS solution. The SVV computation has been carried out on a relatively coarse grid $(N_1, N_2, N_3) = (49, 48, 49)$ with a time step $\delta t = 4 \times 10^{-3}$. The SVV parameters have been chosen equal to $\omega_T = (5\sqrt{N_1}; \sqrt{N_2}; 5\sqrt{N_3})$ and $\varepsilon_N = (1/2N_1; 12/N_2; 1/2N_3)$. This choice of parameters corresponds to a compromise between the accuracy of the SVV solution (analyzed

in Section 4) and the stability of our numerical scheme. Although no extensive study was performed on this point, we have observed that the numerical scheme becomes unstable for ω_T larger than $5\sqrt{N}$ and $\sqrt{N}$ in the non-homogenous and homogenous directions, respectively. This anisotropy of the SVV term takes into account both the anisotropy of the flow and of the distribution of points in the different directions. Consequently, both the amplitude and the number of activated modes by SVV are larger in the azimuthal direction than in the other two directions, due to the small wavelength of the instability structures in this direction (see for example experimental measurements of Schouveiler et al. [38]) compared to the homogeneous grid size.

In order to obtain well-resolved DNS results as our reference, the computations required a much finer grid (11.5 times larger) than the SVV ones, $(N_1, N_2, N_3) = (101, 200, 65)$. As a consequence, the time step adopted is one-tenth as large as in the SVV computation with $\delta t = 5 \times 10^{-4}$.

SVV and DNS solutions are first compared in the spectral spaces by plotting the spectrum coefficients of the kinetic energy in the three directions (see Fig. 5). The results show that the most energetic low frequencies are well described by the SVV solution. More precisely, SVV solution slightly alters the low frequencies in (r, z)

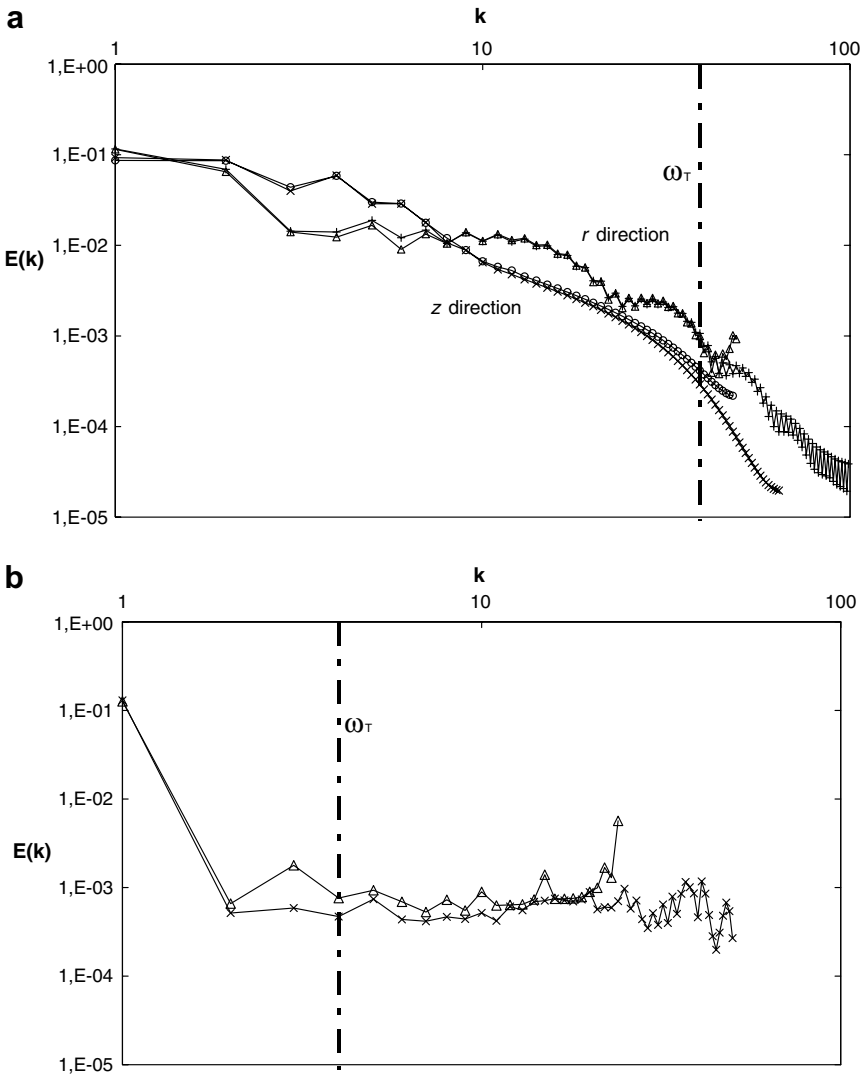

Fig. 5. Spectra of instantaneous spectral coefficients of the kinetic energy corresponding to SVV (triangles and circles) and DNS (crosses) solutions at $Re = 7 \times 10^4$: (a) Chebyshev coefficients in (r, z) directions and (b) Fourier coefficients in θ-direction. Rotor–stator cavity $(R_m = 5, L = 5)$. Log–log plot of a L_2-discrete norm versus the polynomial order.

directions (with an average difference of about 8% in the Chebyshev spectra) and modifies more significantly those in the θ-direction (with an average difference of about 25% in the Fourier spectra), as expected by the use of a more active SVV viscous term. Notice that just between the threshold and the cutoff frequency, these differences increase up to 30% in (r,z) directions and 63% in the θ-direction. Although the SVV is not directly active on these low frequencies, this result is not surprising because SVV modifies the so-called nonlocal triadic interactions. Indeed, the added dissipation alters the contributions from frequencies smaller than the cutoff, and it vanishes those from the frequencies larger (backscatter).

In both SVV and DNS solutions, instabilities within the stationary disk boundary layer are characterized by $n = 4$ pairs of propagating rolls in the mean flow direction. The radial wavelength ($\lambda_r = (b-a)/n$) measured in both solutions match very well, decreasing with the radius in the range $12 \leqslant \lambda_r/\delta \leqslant 18$, $\delta = (\nu/\Omega)^{1/2}$. In the tangential direction, these rolls expand in spiral arms and annular structures (see Fig. 6) as previously shown in experiments by Schouveiler et al. [38] in a rotor–stator cavity of aspect ratio $R/H = 8.75$, at $Re = 20{,}000$. These vortices have been characterized in both solutions using the Q-criterion of Hunt et al. [42] which defines a vortex as a spatial region where the Euclidian norm of the vorticity tensor dominates that of the rate of strain. The DNS solution (see Fig. 6a) shows a complex structure of the flow with many spiral arms that rotate in the same direction as the mean flow driven by the rotor and break through dislocation phenomena. The spiral wave front forms a positive angle with the geostrophic azimuthal flow, decreasing with the radius over the range $\alpha \in [5^\circ; 22^\circ]$. Thus, the spiral arms turn into nearly annular flow next to the inner cylinder. As would be expected, SVV solution (Fig. 6b) shows a more regular structure with spiral

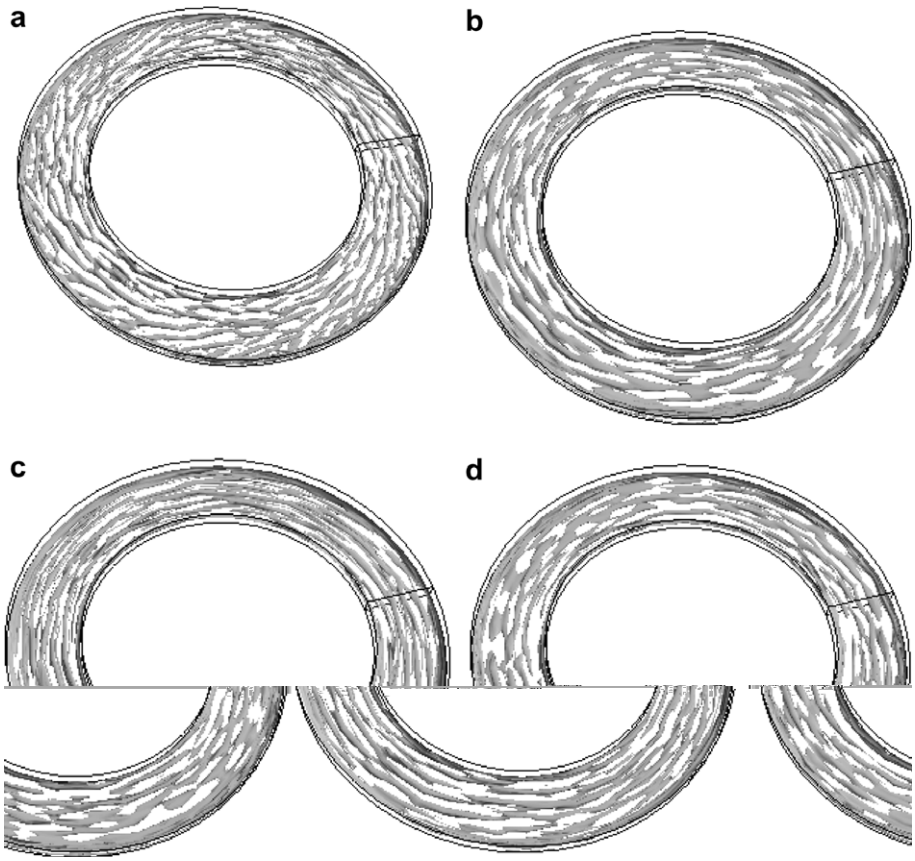

Fig. 6. Structure of instabilities within the turbulent Bödewadt layer at $Re = 7 \times 10^4$. Rotor–stator cavity ($R_m = 5, L = 5$). Iso-surface 3×10^{-2} of the Q-criterion within the stationary disk layer: (a) DNS result on the $101 \times 200 \times 65$ mesh, (b) SVV result with parameters $\omega_T = (5\sqrt{N_1}; \sqrt{N_2}; 5\sqrt{N_3})$ and $\varepsilon_N = (1/2N_1; 12/N_2; 1/2N_3)$ on the $49 \times 48 \times 49$ mesh, (c) DNS result interpolated on the coarser $49 \times 48 \times 49$ mesh and (d) SVV result with parameters $\omega_T = (\sqrt{N_1}; \sqrt{N_2}; \sqrt{N_3})$ and $\varepsilon_N = (1/2N_1; 12/N_2; 1/2N_3)$.

arms of much smaller angle ($\alpha \simeq 4^\circ$). That is easily explained by the coarse resolution in the azimuthal direction ($N_2 = 48$) that is inadequate to accurately capture the spiral pattern obtained by DNS. This result is supported by our filtered DNS, obtained by interpolating the DNS results on the coarse SVV mesh, which shows a very similar flow structure (see Fig. 6c). The solution is weakly sensitive to a variation of the SVV parameters as illustrated in Fig. 6d with $\omega_T = (\sqrt{N_1}; \sqrt{N_2}; \sqrt{N_3})$ and $\varepsilon_N = (1/2N_1; 12/N_2; 1/2N_3)$. More generally and as expected, a decrease of the threshold frequency ω_T in the range $O(\sqrt{N})$ involves a slight decrease of the Q-maxima (less than 5%).

The statistical data have been averaged both in time and in the homogeneous tangential direction. The statistical steady state is expected to be reached when the fluctuations of the averaged values in time are less than 1%. It is of Batchelor type, qualitatively similar to the one presented on Fig. 4.

In spite of the differences observed above in the instability structures developing in the azimuthal direction, there is a close agreement of the mean flow. There is a very good agreement between the axial profiles of the mean tangential and radial velocities across the gap at mid-radius (see Fig. 7). The uniform error of the dif-

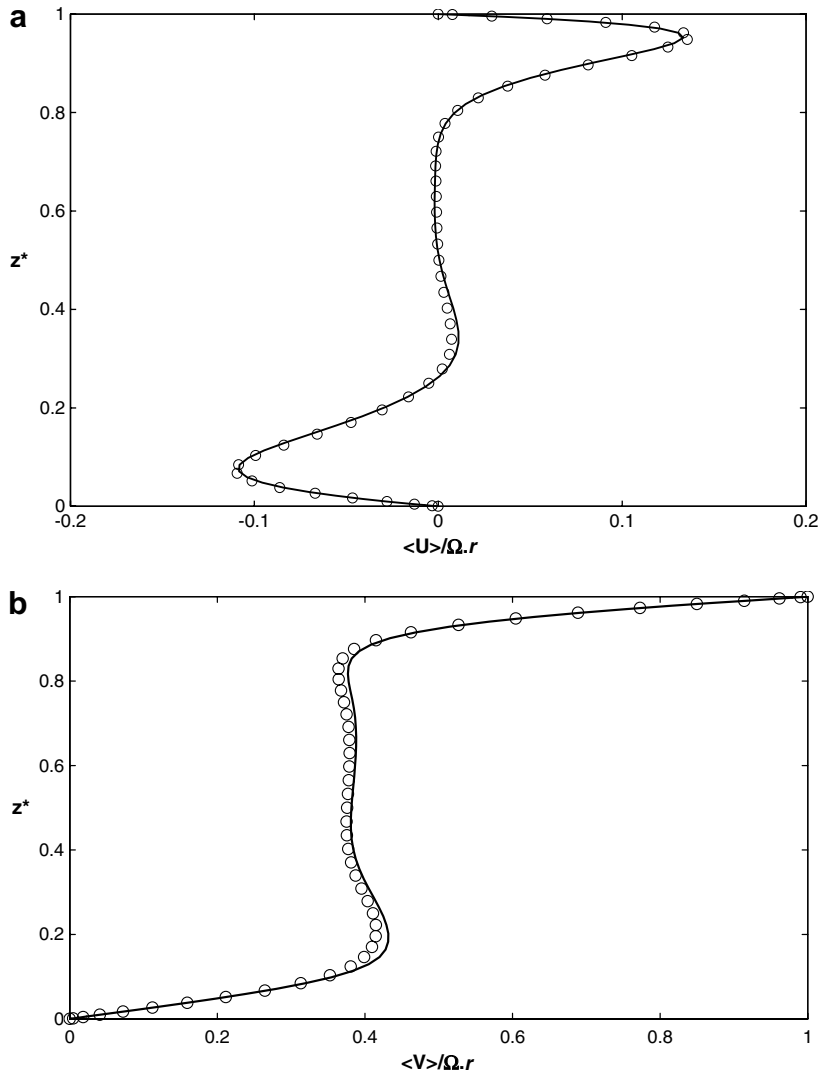

Fig. 7. Axial profiles at $Re = 7 \times 10^4$ of the radial (a) and azimuthal (b) components of the mean velocity at mid-radius, showing a Batchelor mean flow (normalized by the local velocity of the rotor Ω_r). Rotor–stator cavity ($R_m = 5, L = 5$). The crosses correspond to the DNS solution ($101 \times 200 \times 65$ mesh) and, the black circles correspond to the SVV solution ($49 \times 48 \times 49$ mesh).

ference is equal to 3.36% and 0.91% for the radial and the azimuthal mean velocity, respectively. The difference in the thickness and shape of the radial velocity profile near the two disks confirms that the stator layer is already turbulent at mid-radius while the rotor layer remains laminar as expected at this rotation. That is the primary reason that the core circumferential velocity is only about one third ($0.32\Omega_r$) of that of the rotor at the same radius which is very close to the value predicted by the similarity solution, $0.313\Omega_r$ [41]. This result is also supported by Fig. 8a and b where the distributions of turbulent kinetic energy are shown in the meridian plane. Their values are close with the value for the SVV solution, about 8% smaller (7.51×10^{-3} and 8.23×10^{-3}, for the SVV and DNS solutions, respectively). This shows that the additional dissipation introduced though the SVV-operator only slightly affects the global level of turbulence within the cavity. Moreover, the SVV solution provides the right location of the maximum, where the jet flow coming from the rotor impacts the stator.

According to these results, the agreement on the flow characteristics obtained at $Re = 7 \times 10^4$ between the SVV solution and a reference DNS solution requiring a 11.5 times larger grid is very satisfying.

5.2. Turbulent rotor–stator flows at $Re = 4 \times 10^5$ and $Re = 7 \times 10^5$

We demonstrate here the capability of SVV to simulate turbulent rotor–stator flow where the rotating disk layer is now also turbulent over a large radius. The geometrical parameters of the cavity ($R_m = 1.8, L = 5$) have been chosen to correspond to experimentals in order to satisfy both numerical constraints and experimental conditions (Poncet and Chauve, private communication 2006). In order to consider the most unstable

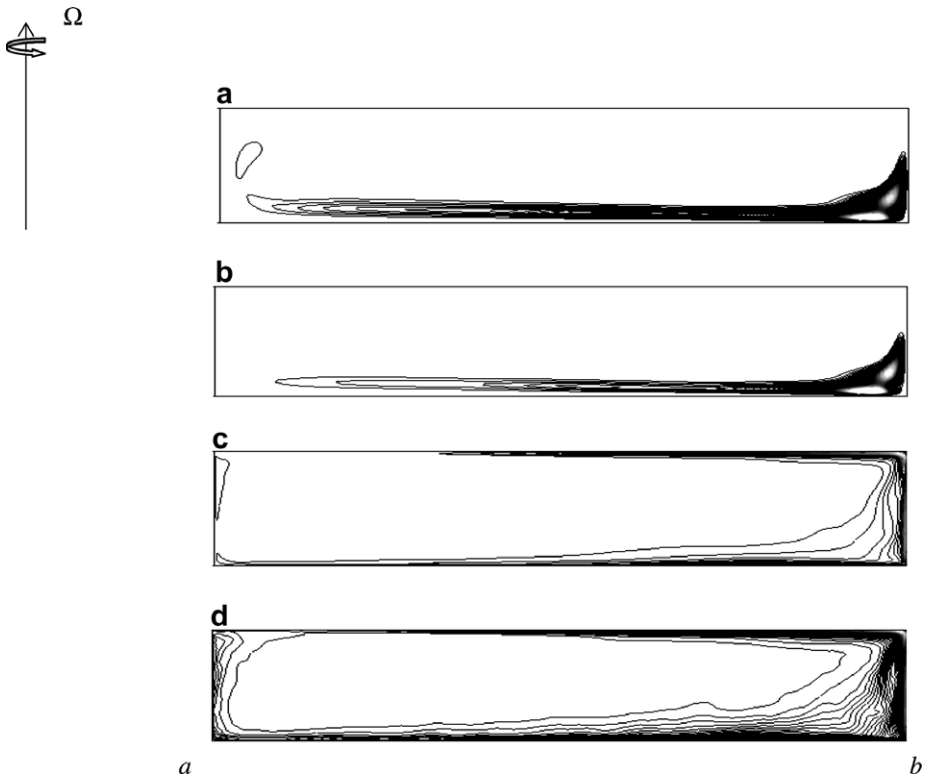

Fig. 8. Isocontours of the turbulent kinetic energy in the meridian plane $(r, z, 0)$ showing the location of turbulent flow regions for different cases: (a, b) Flow in the rotor–stator cavity ($R_m = 5, L = 5$) at $Re = 7 \times 10^4$ showing a turbulent stator layer and a laminar rotor-layer. (a) DNS result on the $101 \times 200 \times 65$ mesh (maximum value, 8.23×10^{-3}). (b) SVV result ($\omega_T = (5\sqrt{N_1}; \sqrt{N_2}; 5\sqrt{N_3})$ and $\varepsilon_N = (1/2N_1; 12/N_2; 1/2N_3)$) on the $49 \times 48 \times 49$ mesh (maximum value, 6.87×10^{-3}). (c, d) Flow in the rotor–stator cavity ($R_m = 1.8, L = 5$). SVV results ($\omega_T = (\sqrt{N_1}; \sqrt{N_2}; 5\sqrt{N_3})$ and $\varepsilon_N = (1/2N_1; 1/N_2; 1/2N_3)$) on the $121 \times 180 \times 65$ mesh: (c) $Re = 4 \times 10^5$ (maximum value, 1.1×10^{-2}) and, (d) $Re = 7 \times 10^5$ (maximum value, 2.12×10^{-2}).

configuration, the external cylinder is at rest while the inner cylinder is rotating with the rotor. The SVV computation has been carried out on a grid $(N_1, N_2, N_3) = (121, 180, 65)$ with a time step $\delta t = 5 \times 10^{-5}$. For the same reasons as in the previous case, the SVV parameters have been chosen equal to $\omega_T = (\sqrt{N_1}; \sqrt{N_2}; 5\sqrt{N_3})$ and $\varepsilon_N = (1/2N_1; 1/N_2; 1/2N_3)$. As shown in Section 3.2, the SVV method retains the fast time integration of our DNS scheme because it is condensed in pre-processing jobs. A reasonable extra computational cost here comes from the occurrence of complex eigenvalues requiring the use of complex FFT. The second-order derivative operators for the pressure calculations have 28 complex conjugate eigenvalues. On the supercomputer Nec SX5, the cpu time per iteration is about 3.2 s while the memory required is 1.1 Giga octets. For these computational parameters the performance of the code is high, about 4.5 Giga Flops, using more than 50% of the peak performance of the vectorial processor.

5.2.1. Flow structures

At these high Reynolds numbers, the turbulent motion is now not just confined to the vicinity of the stationary disk but extends over a large part of the rotating disk as well as along the inner rotating cylinder at the largest value of Reynolds number $Re = 7 \times 10^5$. This is clearly shown by the distribution of turbulent kinetic energy in the meridian plane (r, z) in Fig. 8c and d. With increasing Reynolds number, the maximum turbulent kinetic energy has moved from the stator side (see Fig. 8a at $Re = 7 \times 10^4$) to the end of the rotor side, at the junction between the rotating disk and the stationary outer cylinder, where the radial and tangential velocity components are the largest.

The flow consists of rather tangled co-rotating vortices which originate near the shroud and move radially inward on the stator (outward on the rotor) following the main flow direction. The growth of these vortices strongly affects not only the structure of the two disk boundary layers (see Fig. 9) but also the geostrophic core. This is revealed in Fig. 9a and b by plotting the isocontours of the fluctuations of axial velocity as well as the Q-criterion in the meridian plane at $Re = 7 \times 10^5$. Fig. 9 shows that in the vicinity of the inner and outer cylinders there is now a strong mixing between both boundary layers, involving a large number of vortices of different scales. This underlines the important effects that the inner and outer cylinders have on the characteristics of the turbulence. Notice that the rotating inner cylinder has a strong destabilizing effect (contrary to the configuration where the inner cylinder is stationary [43]), accelerating the flow and strengthening the vortices coming from the Bödewadt layer to the Ekman layer of the rotating disk.

Coherent vortical structures in the near-wall regions are accurately described by the SVV solution at $Re = 7 \times 10^5$ (Fig. 10). In the stator layer, where the turbulence intensity is globally high, the Q-criterion

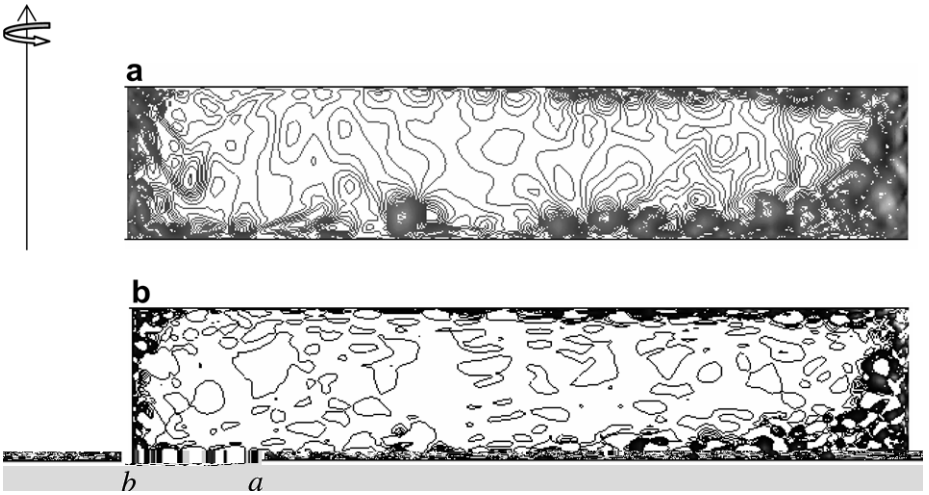

Fig. 9. Flow in the meridian plane $(r, z, 0)$ of the rotor–stator cavity $(R_m = 1.8, L = 5)$ at $Re = 7 \times 10^5$. SVV results $(\omega_T = (\sqrt{N_1}; \sqrt{N_2}; 5\sqrt{N_3})$ and $\varepsilon_N = (1/2N_1; 1/N_2; 1/2N_3))$ on the $121 \times 180 \times 65$ mesh. (a) Isocontours of the fluctuations of the axial component of the velocity $(-9 \times 10^{-2} \leqslant w'/\Omega b \leqslant 2 \times 10^{-2})$. (b) Positive isocontours $(0 \leqslant Q \leqslant 0.98)$ of the Q-criterion showing regions where rotation dominates strain in the flow.

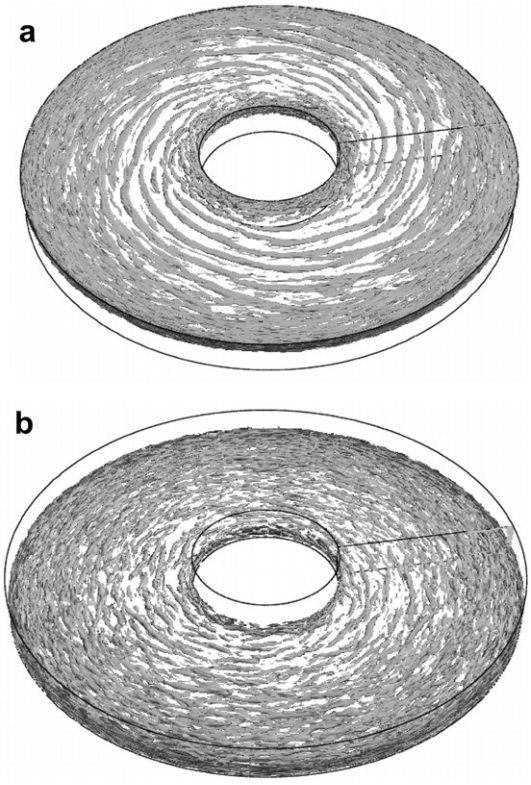

Fig. 10. Coherent vortex in the rotor and the stator layers. Iso-surface $Q = 0.3$ at $Re = 7 \times 10^5$. SVV results ($\omega_T = (\sqrt{N_1}; \sqrt{N_2}; 5\sqrt{N_3})$ and $\varepsilon_N = (1/2N_1; 1/N_2; 1/2N_3)$) on the $121 \times 180 \times 65$ mesh: (a) Transitional turbulent rotor layer and (b) Turbulent stator layer.

shows elongated structures nearly aligned in the tangential direction as already observed in experiments by Little and Eaton [4] and in DNS by Lygren and Andersson [8] near the rotating disk. In the rotor layer, similar structures are found within regions where the turbulence level is high (i.e. at large radius and at the impact of the flow above the inner cylinder). In the middle, where the flow is transitional turbulent ($\sqrt{Re_r} < 500$), the Q-criterion shows large spiral arms. The characteristic parameters of this structure are close to those found for the Type I instability, which is thought to play a role in the transition process to turbulence: averaged values of wavelength and angle with respect to the tangential velocity of are measured equal to $\lambda_r/\delta \simeq 11$ and $\alpha \simeq 8^\circ$, respectively. This result is consistent with results found in linear stability analysis by Serre et al. [44].

5.2.2. Mean field and turbulence statistics

Numerical and experimental axial profiles of the mean radial and tangential velocities are given in Fig. 11 at mid-radius. For both Reynolds numbers, the mean flow is broadly a Batchelor flow as in the laminar regime. The mean axial velocity is not measurable from experiments, and the SVV solution shows it is very small compared to the two other components.

At $Re = 4 \times 10^5$, the agreement between the simulation and the experiment is very satisfying. The angular frequency of the fluid is of about $0.36\Omega_r$ in the core with a difference smaller than 2 between SVV solution ($0.363\Omega_r$) and experimental measurements ($0.356\Omega_r$). The shape of the radial velocity component profiles close to the stator suggests a turbulent layer while on the rotor side the shape remains closer to the laminar solution, suggesting a weakly turbulent flow at mid radius (i.e. $Re_r = 1.7 \times 10^5$ that is less than the value $Re_{rcritical} = 3.6 \times 10^5$ found experimentally by Itoh et al. [37] for a turbulent Ekman layer).

The stator layer thickness is well described by the SVV solution with the crossing $U = 0$ calculated at $z/H = 0.84$ in the SVV solution and measured at $z/H = 0.87$ in experiment. The predicted mean radial velocity has a peak value of $0.086\Omega_r$ located at $z/H = 0.02$, compared to the peak location $z/H = 0.035$ in the

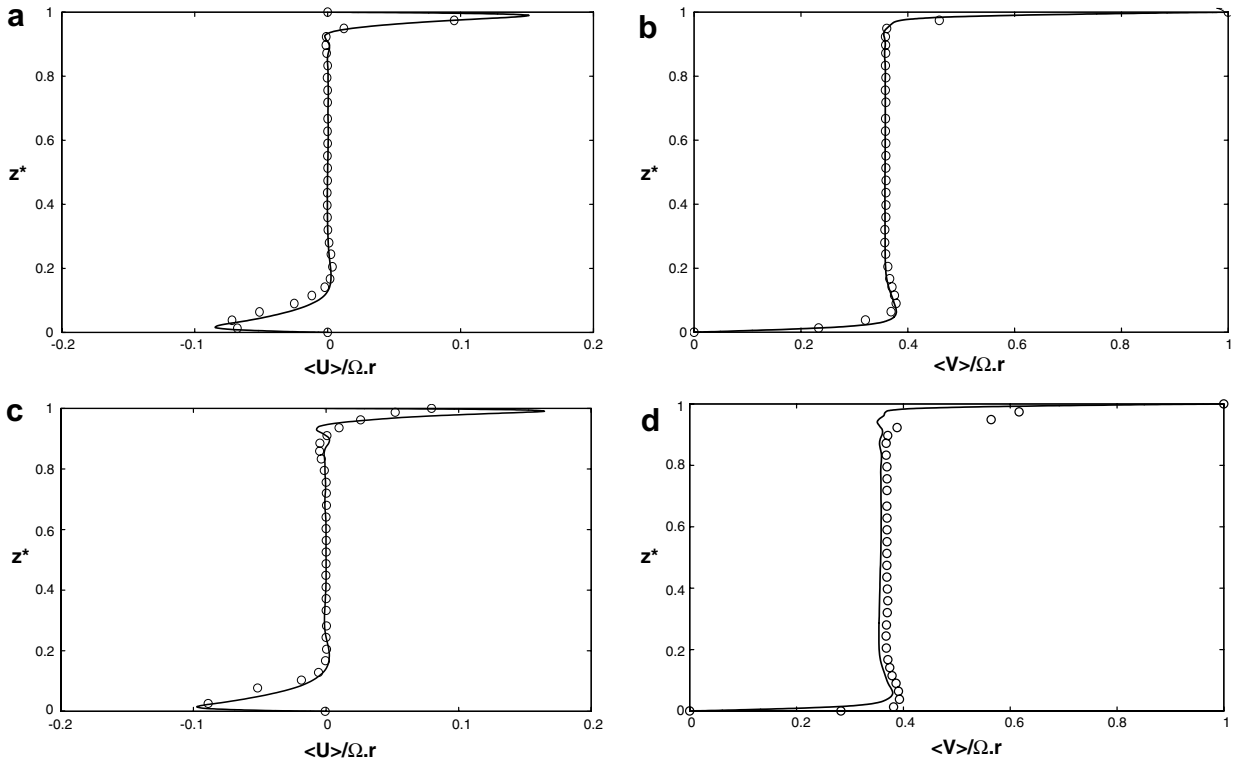

Fig. 11. Comparison of statistical data between experiments (white circles) and SVV-calculations at $Re = 4 \times 10^5$ (a, b) and $Re = 7 \times 10^5$ (c, d). Axial profiles of the radial (a, c) and azimuthal (b, d) components of mean velocity at mid-radius, normalized by the local velocity of the rotor Ω_r.

experiments. The maximum error in the mean radial velocity occurs near the location of the peak crossflow with a magnitude less than $0.01\Omega_r$. The measurements on the rotor side are technically much more difficult and consequently there are only few points. Nevertheless, the radial velocity values at the two points near the rotating disk fit very well with the SVV solution that gives a good description of the Ekman layer thickness.

Second-order statistics available from experimental measurements in the streamwise and spanwise directions have been computed. The square roots of two of the main Reynolds stresses ($\overline{V'_r V'_r}$ and $\overline{V'_\theta V'_\theta}$) have been normalized by the local speed of the disk and are shown in Fig. 12. The third shear stress $\overline{V'_\theta V'_r}$ is of negligible importance, with a magnitude two-order lower than the previous Reynolds stresses, as already obtained in DNS by Lygren and Andersson [8]. The general trend is that the experimental and numerical data match quite well for the two normal Reynolds stresses. Although the turbulence intensity is weak within the core, it is well-predicted by SVV solution. As with the mean flow, the maximum error occurs in the prediction of the peak values near the walls. On the stator side, there is a relatively large overprediction in the streamwise direction with a magnitude of about $0.025\Omega_r$ and a small underprediction in the radial direction with a magnitude less than $0.006\Omega_r$. Near the rotor, the experimental values are lower than the simulated ones. Moreover, the predicted turbulence intensity is higher on the rotor than in the stator while in experiment the turbulence intensity is almost the same near the two disks. This trend was previously observed in DNS by Lygren and Andersson [8] in a cavity of infinite radial extension, particularly when the stresses are not normalized by the wall friction velocity. Nevertheless, the reasoning invoked by these authors and related to the fact that the experimental cavity of Itoh et al. [37] is closed, cannot be used here where the cavities are similar. Moreover, the difference closures at the junction between the rotating and stationary parts (a small clearance is used in experiment versus a regularized profile imposed in the numerical approach) seem difficult to invoke here. The most likely reason is related to the anisotropy of the grid computation, which is globally much coarser in the tangential

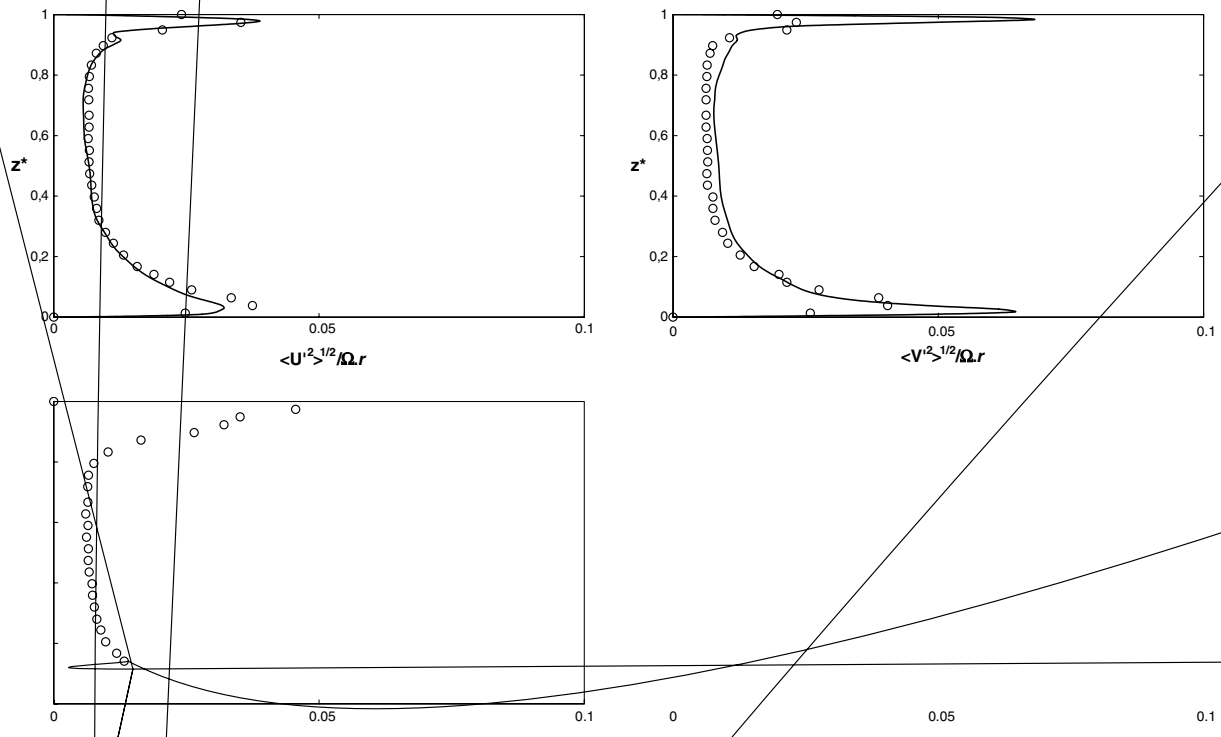

direction than in two other directions: the grid spacing in the tangential direction at mid radius is $0.16H$ while the averaged grid spacing (the grid is non-homogeneous and tighter close to the walls) in the radial and axial directions is about $4.1 \times 10^{-2}H$ and $1.5 \times 10^{-2}H$, respectively. This reasoning was already proposed by Scotti et al. [45] to explain some discrepancies between LES calculations of wall-bounded flows and experiments. This phenomenon could certainly be reduced with grid refinement in the streamwise direction.

As a consequence, the predicted Reynolds stress tensor is more anisotropic than the measured one, with a maximum in streamwise direction about two times larger than in the radial direction.

At $Re = 7 \times 10^5$ and keeping the same numerical resolution, there is still an overall agreement between calculations and measurements although it is not as good as at $Re = 4 \times 10^5$, as expected due to an increase greater than 50% in the value of the Reynolds number. This is particularly true for the prediction of the tangential mean velocity in the core Fig. 11d. The predicted angular frequency of the fluid remains about the same in the core as at $Re = 4 \times 10^5$ (about $0.36\Omega_r$), while in experiment the angular frequency has increased measurably up to $0.39\Omega_r$.

Surprisingly, the turbulent stator layer thickness is still well described by the SVV solution. However, the shape of the radial component profiles measured in experiments on the rotor side suggest now a turbulent layer, while the estimated profile remains close to the laminar solution. This overall trend is supported by the second-order statistics profiles. These results suggest as expected that the SVV calculation is no longer able to account for the increase in turbulence intensity in the rotor layer induced by the increase in rotation. The SVV calculation is now too dissipative, the magnitude of the SVV operator being too large compared to the magnitude of the viscous operator, which has decreased with the increase in Reynolds number. An estimation of this can be given by the mean value s, defined as the dissipated energy ratio of our model with respect to the total dissipation:

$$s = \left\langle \frac{\|\mathbf{V}_{N_i} \cdot \nabla \cdot (\varepsilon_{N_i} Q_{N_i}(\nabla \mathbf{V}_{N_i}))\|_2}{\|\mathbf{V}_{N_i} \cdot \Delta_{\mathrm{SVV}}(\mathbf{V}_{N_i})\|_2} \right\rangle \tag{37}$$

where the brackets indicate a temporal averaging. Thus at $Re = 4 \times 10^5$, $s = 0.4$ while it almost doubles, $s = 0.7$, at $Re = 7 \times 10^5$. Notice as a reference that for $s = 1$, the dissipation would be totally ensured by the SVV term.

6. Concluding remarks

The highly accurate computation of turbulent rotating flows within cavity is of interest for both engineering applications with turbomachinaries, and fundamental research, as one of the simplest cases where the turbulent boundary layers are three-dimensional. Such flows are difficult to compute when using spectrally accurate numerical schemes, that results directly from the fact that spectral approximations are much less diffusive than low order ones.

We have proposed in this paper a spectral vanishing viscosity method that stabilizes the incompressible three-dimensional Navier–Stokes equations in a cylindrical domain. Associated with spectral methods, this method appears of interest for the investigation of turbulent rotating flows, by providing solutions that converge to solutions of Navier–Stokes equations when the cuttoff goes to infinity, and by preserving the spectral accuracy of smooth solutions. As formerly outlined in the literature, this method may be viewed as an alternative LES approach (more precisely a no-model spectral LES approach, i.e. no modeling of the subgrid-scale tensor), in the sense of directly computing the large energetic scales while controlling the smaller scales.

An algorithm has been proposed in the frame of 3D spectral Chebyshev–Fourier computations, well adapted to the LES of turbulent rotating flows within interdisk cavities. It should be mentioned that this method does not require additional computational time, the SVV operator being included in the viscous term and that the problem of the commutation error between the differentiation and the filtering operators no longer arises. Confined rotating flows are strongly inhomogeneous and anisotropic, due to the coupled effect of rotation and confinement, and consequently the modeling of the subgrid-scale tensor, which results from the spatial filtering of the Navier–Stokes equations, still remains a very challenging task. Besides, at our knowledge, LES of such flows do not exist in the literature.

First, a study of the convergence properties of the algorithm has been provided using an analytical solution. Different sets of SVV parameters have been considered, and in all cases it has been shown that the exponential property of spectral method is preserved although if the convergence rate can worsen. Second, to demonstrate the efficiency of the SVV to perform LES of turbulent rotating flows, rotor–stator flows have been considered for Reynolds numbers ranging between 7×10^4 to 7×10^5. The structure of these flows is highly complex involving laminar, transitional, and turbulent flow regions. Indeed, the stationary disk layer is much more unstable than the rotor boundary layer, and both are separated by a very stable non-viscous rotating core. Mean profiles have been provided at $Re = 7 \times 10^4$ and match very well with a DNS which required a 11.5 times larger mesh. At high Reynolds numbers ($Re = 4 \times 10^5$ and $Re = 7 \times 10^5$), where DNS results are unreachable, mean profiles and two of normal Reynolds stresses ($\overline{V'_r V'_r}$ and $\overline{V'_\theta V'_\theta}$) have been shown to compare favorably with experimental measurements obtained in the same cavity.

In this frame of SVV-pseudo-spectral method, all these results are very encouraging to perform now LES of turbulent rotating flows within cavities, and thus provide additional contributions to their highly accurate computations.

Acknowledgements

The authors acknowledge the IDRIS (CNRS) computing center (Program 050242). The authors gratefully acknowledge S. Poncet and M.P. Chauve (CNRS/ IRPHE laboratory) who provided us with their experimental data. The authors are very grateful to Professors R. Pasquetti (CNRS/ Lab. J. Dieudonné Nice) and B.E. Launder (Univ. of Manchester) for fruitful discussions. The work was supported by CNRS in the frame of the DFG-CNRS program "LES of complex flows". Support for E. Séverac by a CNRS grant is also acknowledged.

References

[1] J.M. Owen, R.H. Rogers, Flow and heat transfer in rotating-disc systems, Rotor–Stator Systems, vol. 1, Research Studies Press, Taunton, 1989.
[2] G.N. Coleman, G.H. Ferziger, P.R. Spalart, A numerical study of the turbulent Ekman layer, J. Fluid Mech. 213 (1990) 313.
[3] H.S. Kang, H. Choi, J.Y. Yoo, On the modification of the near-wall coherent structure in a three-dimensional turbulent boundary layer on a free rotating disk, Phys. Fluids 10 (9) (1998) 2315.
[4] H.S. Little, J.K. Eaton, Turbulence characteristics of the boundary layer on a rotating disk, J. Fluid Mech. 266 (1994) 175.
[5] E. Serre, E. Crespo del Arco, P. Bontoux, Annular and spiral patterns in flows between rotating and stationary discs, J. Fluid Mech. 434 (2001) 65.
[6] S. Poncet, A. Randriamampianina, Turbulence characteristics of the Bödewadt layer in a large enclosed rotor–stator system, Phys. Fluids (2006) 18.
[7] E. Serre, P. Bontoux, B.E. Launder, Transitional-turbulent flow with heat transfer in a closed rotor–stator cavity, J. Turbulence 5 (2004) 008.
[8] M. Lygren, H. Andersson, Turbulent flow between a rotating and a stationary disk, J. Fluid Mech. 426 (2001) 297.
[9] H. Iacovides, I.P. Theofanoupolos, Turbulence modelling of axisymmetric flow inside rotating cavities, Int. J. Heat Fluid Flow 12 (1991) 2.
[10] B.E. Launder, D.P. Tselepidakis, Application of a new second moment closure to turbulent channel flow rotating in orthogonal mode, Int. J. Heat Fluid Flow 15 (1994) 2.
[11] V. Borue, S. Orzag, Locally energy flux and subgrid-scale statistics in three-dimensional turbulence, J. Fluid Mech. 326 (1998) 1.
[12] M. Lesieur, O. Métais, New trends in large-eddy simulation, Annu. Rev. Fluid. Mech. 28 (1996) 45.
[13] J. Bardina, J.H. Ferziger, W.C. Reynolds, Improved turbulence models based on large eddy simulation of homogeneous (incompressible) turbulent flows, Report TF19, Thermoscience Division, Department of Mechanical Engineering, Stanford University, 1983.
[14] S. Stolz, N.A. Adams, L. Kleiser, An approximate deconvolution model for large eddy simulation with application to incompressible wall-bounded flows, Phys. Fluids 13 (4) (2001) 2985.
[15] K. Horiuti, A new dynamic two-parameter mixed model for large eddy simulation, Phys. Fluids 9 (1997) 3443.
[16] X. Wu, K.D. Squires, Prediction and investigation of the turbulent flow over a rotating disk, J. Fluid. Mech. 418 (2000) 231.
[17] M. Germano, U. Piomelli, P. Moin, W.H. Cabot, A dynamic subgrid-scale eddy viscosity model, Phys. Fluids A 29 (1991) 1760.
[18] Y. Zang, R. Street, J.R. Koseff, A dynamic mixed subgrid-scale model and its application to turbulent recirculating flows, Phys. Fluids 5 (1993) 3186.
[19] B. Vreman, B. Geurts, H. Kuerten, On the formulation of the dynamic mixed subgrid-scale model, Phys. Fluids 6 (1994) 4057.
[20] M. Lygren, H. Andersson, Large eddy simulation of the turbulent flow between a rotating and a stationary disk, ZAMM 55 (2004) 268.
[22] J.L. Guermond, J.T. Oden, S. Prudhomme, Mathematical perspectives on large eddy simulation models for turbulent flows, J. Math. Fluid Mech. 6 (2004) 194.
[23] C. Fureby, F.F. Grinstein, Monotonically integrated large eddy simulation of free shear flows, AIAA J. 37 (5) (1999) 19.
[24] R. Peyret, Spectral methods for incompressible viscous flow, Applied Mathematical Sciences, 48, Springer-Verlag, New York, 2002.
[25] E. Serre, J.P. Pulicani, 3D pseudo-spectral method for convection in rotating cylinder, Comput. Fluids 30/4 (2001) 491.
[26] I. Raspo, S. Hugues, E. Serre, A. Randriamampianina, P. Bontoux, Spectral projection methods for the simulation of complex three-dimensional rotating flows, Comput. Fluids 31 (4–7) (2002) 745.
[27] E. Tadmor, Convergence of spectral methods for nonlinear conservation laws, SIAM J. Numer. Anal. 26 (1) (1989) 30.
[28] Y. Maday, S.M.O. Kaber, E. Tadmor, Legendre pseudo-spectral viscosity method for nonlinear conservation laws, SIAM J. Numer. Anal. 30 (2) (1993) 321.
[29] O. Andreassen, I. Lie, C.E. Wasberg, The spectral viscosity method applied to simulation of waves in a stratified atmosphere, J. Comput. Phys. 110 (1994) 257.
[30] G.S. Karamanos, G.E. Karniadakis, A spectral vanishing viscosity method for large eddy simulation, J. Comput. Phys. 163 (2000) 22.
[31] R.M. Kirby, S.J. Sherwin, Stabilisation of spectral/*hp* element methods through spectral vanishing viscosity: Application to fluid mechanics modelling, Comput. Methods Appl. Mech. Eng. 195 (2006) 3128.
[32] R. Pasquetti, C.J. Xu, High-order algorithms for large-eddy simulation of incompressible flows, J. Sci. Comput. 17 (1–4) (2002) 273.
[33] J.M. Vanel, R. Peyret, P. Bontoux, A pseudospectral solution of vorticity streamfunction equations using the influence matrix technique, K.W. Morton, M.J. Baines (Eds.), Numerical Methods for Fluid Dynamics II, pp. 463–475, 1986.
[34] R.H. Kraichnan, Eddy viscosity in two and three dimensions, J. Atmos. Sci. 33 (1976) 1521.
[36] E. Crespo del Arco, E. Serre, P. Bontoux, B.E. Launder, Stability, transition and turbulence in rotating cavities, in: M. Rahman (Ed.), Advances in Fluid Mechanics, vol. 41, Dalhousie University Canada Series, 2005.
[37] M. Itoh, Y. Yamada, S. Imao, M. Gonda, Experiments on turbulent flow due to an enclosed rotating disc, Exp. Therm. Fluid Sci. 5 (1992) 359.
[38] L. Schouveiler, P. Le Gal, M.P. Chauve, Y. Takeda, Spiral and circular waves in the flow between a rotating and a stationary disc, Exp. Fluids 26 (1999) 179.
[39] S.A. Orzag, A.T. Patera, Secondary instability of wall-bounded shear flows, J. Fluid Mech. 128 (1983) 347–383.
[40] C. Canuto, M.Y. Hussaini, A. Quarteroni, T.A. Zang, Spectral Methods in Fluids Dynamics, Springer-Verlag, 1988.
[41] J.F. Brady, L. Durlofsky, On rotating disc flow, J. Fluid Mech. 175 (1986) 363.

[42] J.C.R. Hunt, A. Wray, P. Moin, Eddies, stream, and convergences zones in turbulent flows, Center of Turbulent Research Report CTR-S88, 1998.
[43] E. Serre, P. Bontoux, B.E. Launder, Direct numerical simulation of transitional turbulent flow in an enclosed rotor–stator cavity, Int. J. Flow Turbulence Combust. (Kluwer) 69 (2002) 35.
[44] E. Serre, E. Tuliska-Sznitko, P. Bontoux, Coupled theoretical and numerical study of the flow transition between a rotating and a stationary disk, Phys. Fluids 16 (3) (2004) 688.
[45] A. Scotti, C. Meneveau, D.K. Lilly, Generalized Smagorinsky model for anisotropic grids, Phys. Fluids A5 (1993) 2306.